# Supporting Information for Zhao et al.
# doi:10.1073/pnas.1603387113

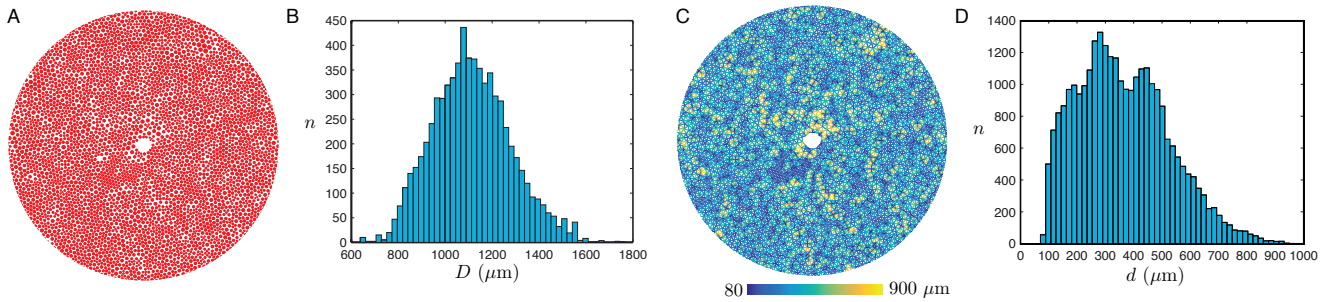


**Fig. S1.** To create the post pattern, we first generate an irregular triangular mesh inside a circle using the `pdemesh` tool in MATLAB. We use the nodes of the triangular mesh as the centers of the posts. We then assign the radius of each post to be 45% of the distance to its nearest neighbor, which provides a random distribution of non-overlapping posts. (A) Post pattern. (B) The post sizes follow a Gaussian distribution that ranges from 600 to 1700 $\mu$m. (C) The spatial distribution of pore-throat sizes. (D) The pore-throat sizes range from 80 to 900 $\mu$m.

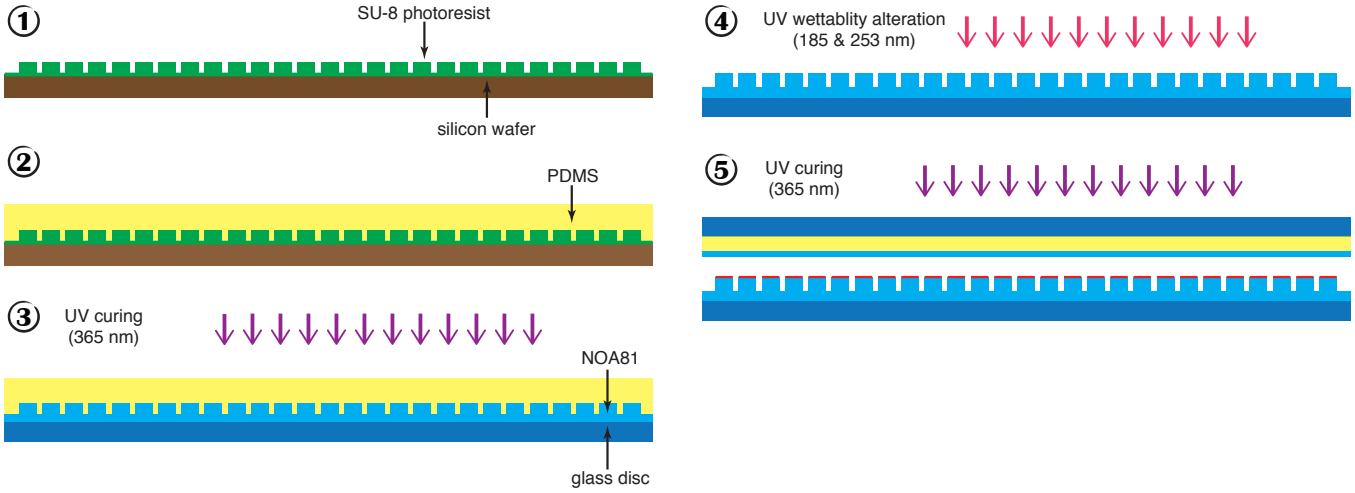


**Fig. S2.** We fabricate the microfluidic flow cells via soft imprint lithography, following the steps illustrated above: (1) We first generate a silicon master of the post pattern via conventional photo-lithography techniques. We spin coat a negative photoresist (SU8-2050, MicroChem, USA) onto a 6" silicon wafer at 1,700 rpm for 30 s to achieve a film thickness of 100 $\mu$m. After soft baking, we expose the photoresist to UV light through a photomask of the post pattern, which selectively polymerizes the photoresist to form the posts. We subject the photoresist to post-exposure-bake, and developed with ethyl lactate to dissolve the unexposed areas of the photoresist. (2) We use the silicon master to create PDMS (Sylgard 184, Dow-Corning, USA) casts of the post pattern. The PDMS cast forms a negative complement of the silicon master, which consists of wells rather than posts. (3) The core of the flow cell is made of a photo-curable polymer (NOA81, Norland Optics, USA) and it consists of a flat top half and a bottom half that contains the post structures. To make the bottom half of the microfluidic cell, we first deposit a puddle of NOA81 onto a 4" glass disc. We allow the NOA81 to spread across the glass disc before carefully covering it with the PDMS cast. Upon contact, the NOA81 spontaneously fills the wells in the PDMS cast. After removing any excess NOA81 with a metal roller, we cure it with a collimated 365 nm UV light source (MA4-1, Karl Suss, Germany) for 15 s at 25 mW/cm$^2$. (4) We peel off the PDMS cast after curing, and subject the NOA81 to wettability alteration (see fig. S3). (5) After wettability alteration, we bind the flat NOA81 piece and the patterned NOA81 piece together with 365 nm UV radiation for 60 s at 25 mW/cm$^2$.

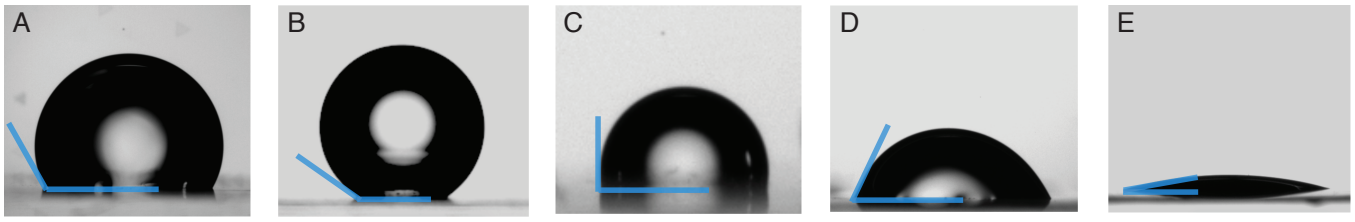


**Fig. S3.** We characterize the wettability of our system by placing a small drop of DI water on a treated NOA81 surface submerged in a silicone oil-filled reservoir. We image the water drop with a contact angle goniometer (model 250, ramé-hart, USA), which measures the water/silicone oil contact angle via its `DROPimage` software. All contact angle measurements are made 24 hrs after treatment, which corresponds to the typical amount of time elapsed between wettability alteration of the flow cell and the fluid-fluid displacement experiment. (A) The contact angle of water on an untreated NOA81 surface immersed in silicone oil is $\theta = 120^\circ \pm 3^\circ$. (B) To make the NOA81 surface more hydrophobic, we apply chemical vapor deposition (CVD) of trimethoxysilane in a desiccator for 30 mins, which yields a contact angle of $\theta = 150^\circ \pm 5^\circ$. To make the NOA81 surface more hydrophilic, we expose it to high-energy UV light in a UV-ozone cleaner (UV-1, Samco, Japan), which generates UV light that peaks at 185 & 253 nm. By varying the duration of UV exposure ($t_{UV}$), we achieve contact angles of (C) $\theta = 90^\circ \pm 7^\circ$ ($t_{UV} = 85$ s), (D) $\theta = 60^\circ \pm 5^\circ$ ($t_{UV} = 210$ s), and (E) $\theta = 7^\circ \pm 3^\circ$ ($t_{UV} = 1800$ s).

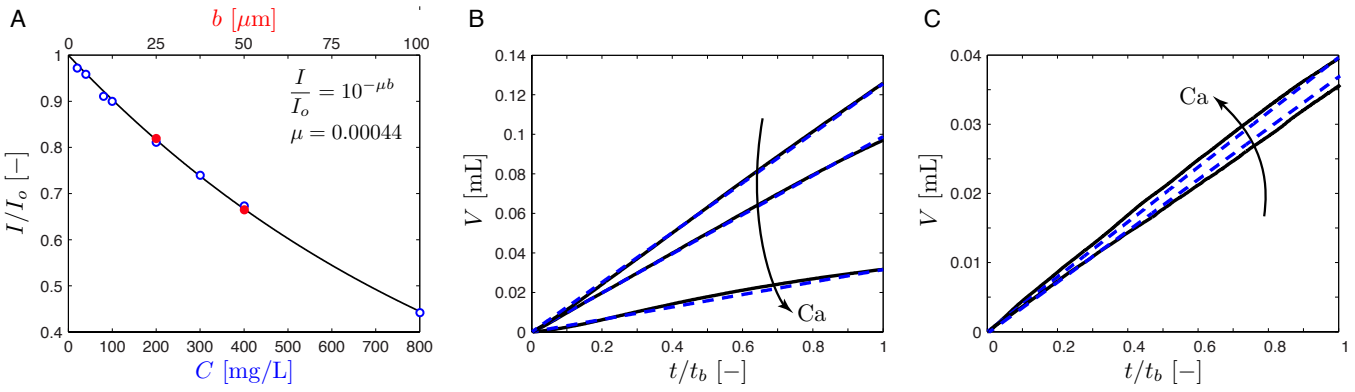


**Fig. S4.** To gain more information about the fluid-fluid displacement in 3D, we seed the injected water with a light absorbing dye (Brilliant Blue G, Alfa Aesar, USA) and measure the gap-averaged water saturation from the transmitted light intensity via a calibration curve. (A) We experimentally generate a calibration curve that relates the normalized transmitted-light intensity $I/I_o$ to the dye concentration $C$ in the water solution (blue circles), which is well-described by the Beer-Lambert law (solid line). We further find an one-to-one relationship in the transmittence of water films of different dye concentrations at a fixed thickness (100 $\mu$m), and water films of different thicknesses at a fixed concentration (800 mg/L; red dots). This allows us to convert the measured transmitted-light intensity to the gap-averaged water saturation. (B – C) We test the accuracy of the quantified water saturation by comparing the injected volume calculated from the images (solid line) with the actual injected volume (dashed line) as a function of normalized time $t/t_b$, where $t_b$ is the amount of time it takes for the invading fluid to reach the edge of the flow cell. We show the comparison here for (B) strong drainage and (C) strong imbibition. We do not show the volume evolution for strong imbibition at $\mathrm{Ca} = 2.9 \times 10^{-1}$ here as it overlaps with strong imbibition at $\mathrm{Ca} = 2.9 \times 10^{-2}$.

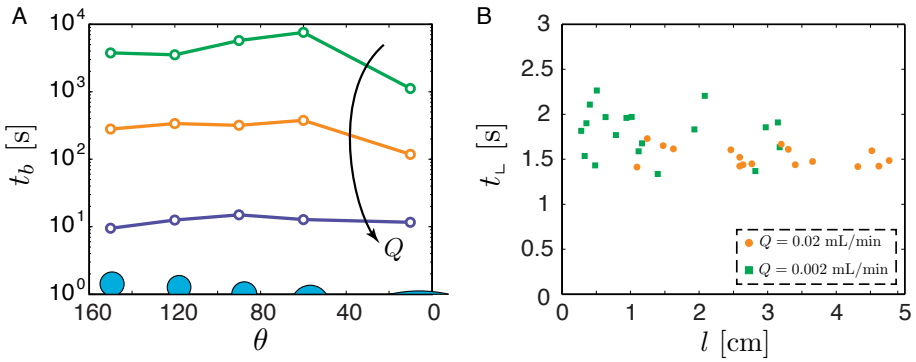


**Fig. S5.** (A) We characterize the macroscopic time scale of the experiments as the breakthrough time $t_b$, which is defined as the amount of time it takes for the displacement front to reach the perimeter of the flow cell. For a given wettability condition, this time scale is controlled by the injection rate $Q$ and is therefore captured by the macroscopic Ca. (B) We characterize the local time scale in strong imbibition as $t_L$, which is defined as the amount time it takes for corner flow to coat a single median-sized post. Here we show $t_L$ for post coating via corner flow at Ca$= 2.9 \times 10^{-2}$ (orange circle) and Ca$= 2.9 \times 10^{-3}$ (green square) as a function of the radial position $l$ where this coating event occurs. We find $t_L \approx 1.5$ s over an order of magnitude change in $Q$.

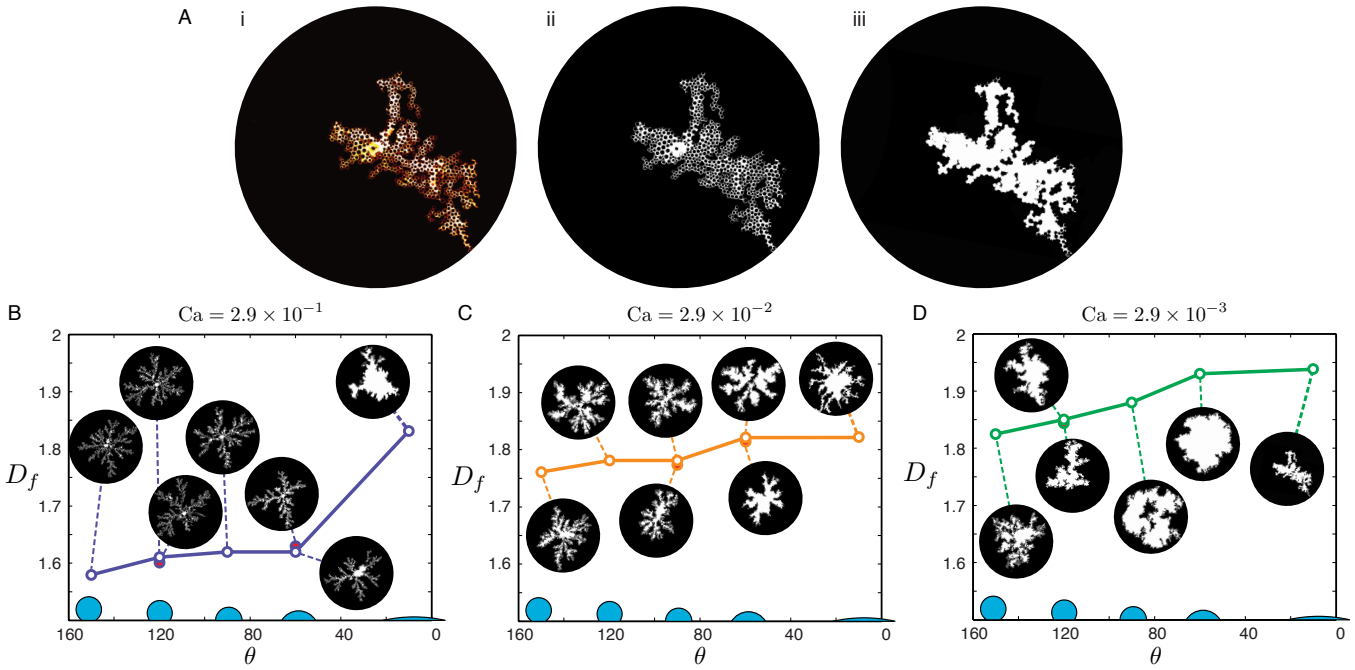


**Fig. S6.** We quantify the invasion patterns in 2D by calculating their fractal dimension $D_f$ via the box-counting method. (A) Example workflow for calculating $D_f$: (i) we first convert the final image of the experiment from intensity to gap-averaged water saturation via the calibration curve; (ii) we then create a binary image of invaded (white) and un-invaded (black) regions by applying a global saturation threshold ($S_{\mathrm{thresh}} \approx 0.01$); (iii) we "fill in" any posts that are completely surrounded by the invading fluid, including these as part of the invaded region. We leave unaltered any regions containing trapped defending fluid. Finally, we calculate $D_f$ for the invaded region via the box-counting method. (B–D) Fractal dimension measurements for the invasion patterns as a function of the static contact angle, with illustrations of the corresponding invaded regions (insets). We find $D_f = 1.58$ for viscous fingering and $D_f = 1.82$ for capillary fingering in strong draiange ($\theta = 150°$), which agree well with values reported in previous studies [refs. 16–18].

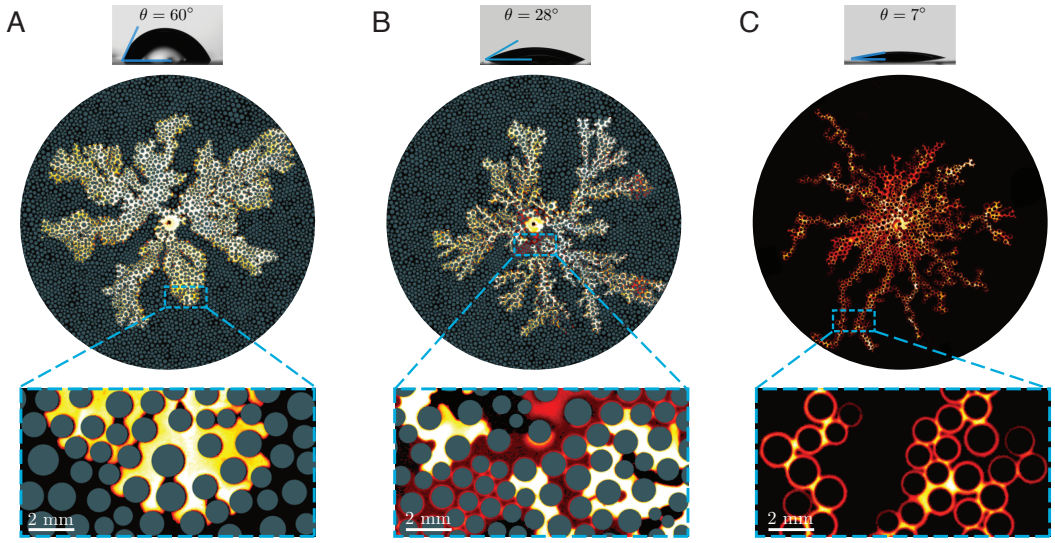


**Fig. S7.** Fluid-fluid displacement patterns for (A) weak imbibition ($\theta = 60°$), (B) an intermediate wetting condition ($\theta = 28°$) between weak imbibition and strong imbibition, and (C) strong imbibition ($\theta = 7°$) at Ca$= 2.9 \times 10^{-2}$. Blue boxes highlight the pore-scale view of the displacement processes. Macroscopically, the displacement pattern in the intermediate wetting condition is less space-filling than weak imbibition, but more space-filling than strong imbibition, in accordance with a critical wetting transition at $\theta_{\llcorner} = 45°$. In weak imbibition, as is the case for strong drainage ($\theta = 150°$), weak drainage ($\theta = 120°$), and neutral ($\theta = 90°$) experiments, the invading fluid advances by displacing the defending fluid from the pore-bodies. This is not the case in strong imbibition, where the invading fluid advances by coating the perimeter of the posts via corner flow, rather than filling the pore bodies. In the intermediate wetting condition ($\theta = 28°$), we observe the co-existence of pore-body displacement and corner flow. This is consistent with the theoretically derived critical contact angle for corner flow of $\theta_{\llcorner} = 45°$. In addition, it is apparent that the width of the corner flow film in the intermediate wetting condition is smaller than that observed in strong imbibition, which is consistent with our analysis that the interface of corner flow will be pushed further into the corner as $\theta \to \theta_{\llcorner}$ (Fig. 4C of the manuscript).